Supplementary Information

Organics Intercalation into Layered Structures Enables Superior Interface Compatibility and Fast Charge Diffusion for Dendrite-Free Zn Anodes

Huili Peng,[a] Changhui Liu,[b] Nana Wang,[c] Chenggang Wang,[a] Dongdong Wang,[a] Yanlu Li,[b] Bo Chen,[d] Jian Yang*[a] and Yitai Qian[ae]

Key Laboratory of Colloid and Interface Chemistry, Ministry of Education, School of Chemistry and Chemical

Engineering, Shandong University, Jinan 250100, PR China
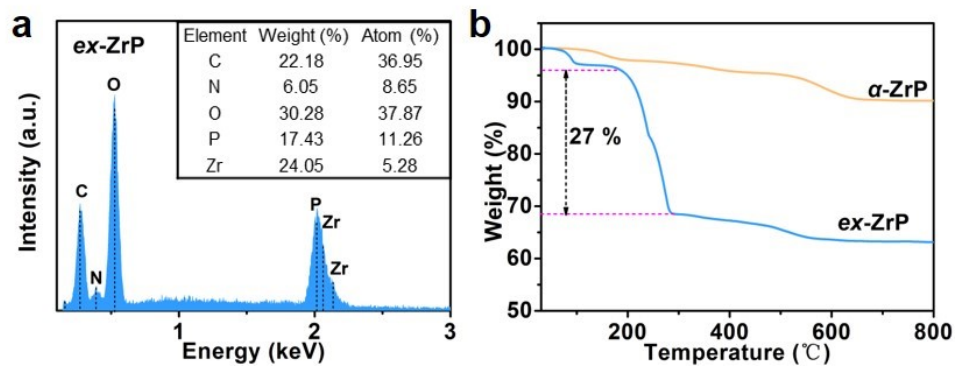
Corresponding Author:

yangjian@sdu.edu.cn

1

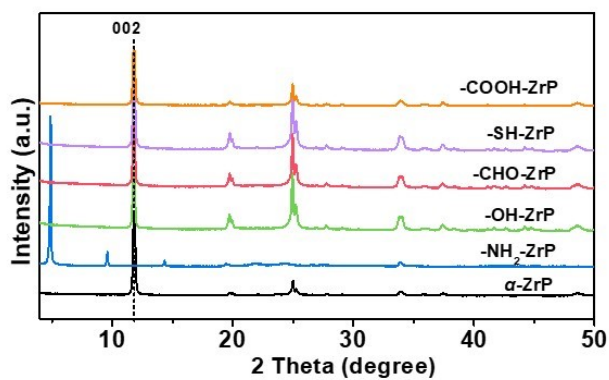**Fig. S1** (a) EDS spectrum of *ex*-ZrP, (b) TGA curves of *α*-ZrP and *ex*-ZrP.

Fig. S2 XRD patterns of *ex*-ZrP treated by butanol (-OH), butanal (-CHO), butanethiol (-SH) or butyric acid (-COOH).
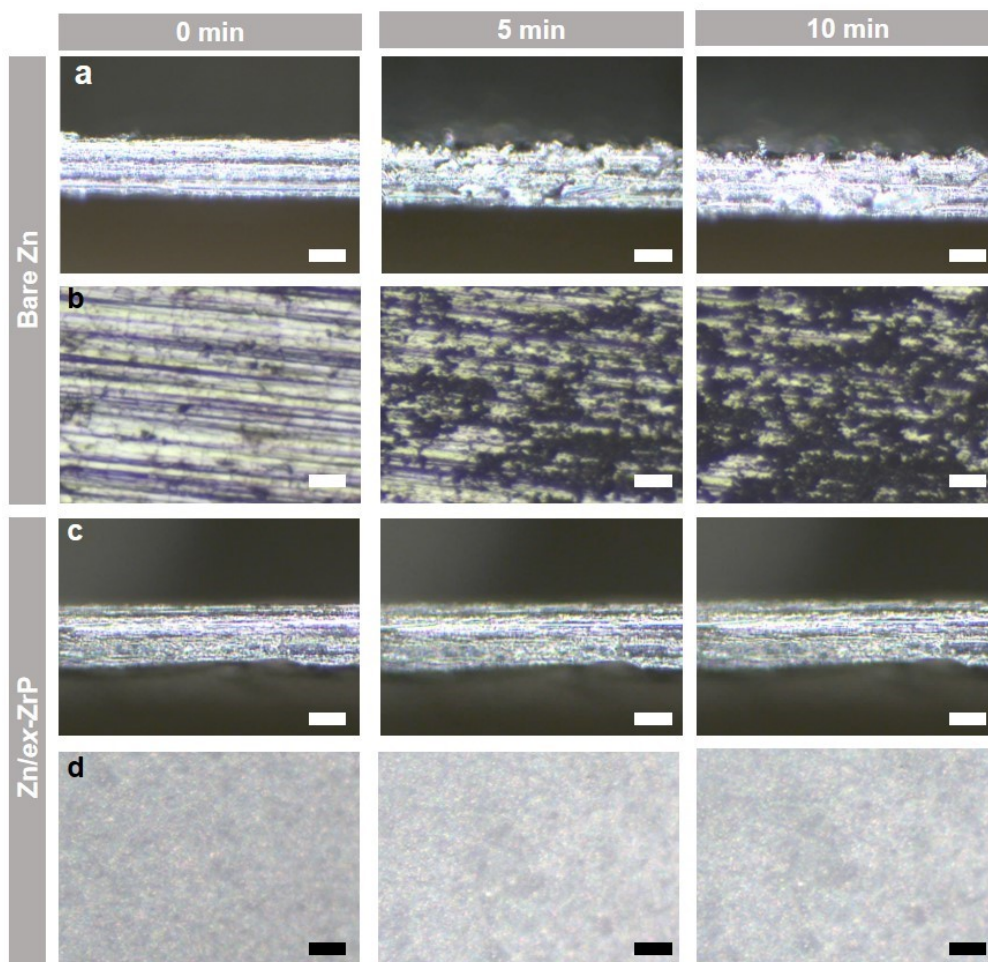
Fig. S3 *In-situ* optical microscope imaging of the electrochemical plating of Zn on bare Zn and Zn/*ex*-ZrP at 6 mA cm^{-2}. (a, c) cross-section images and (b, d) top-view images. Scale bars: 20 μm.
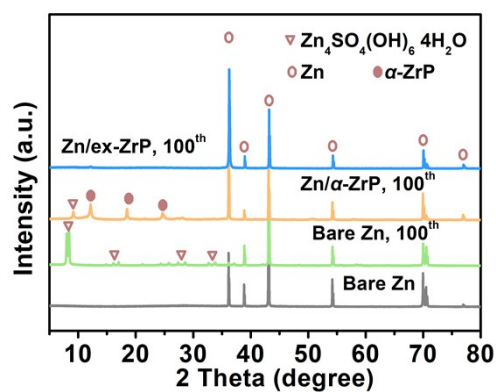

Fig. S4 XRD patterns of bare Zn, Zn/α-ZrP and Zn/*ex*-ZrP after 100 cycles in the symmetric cells at 6 mA cm^{-2} for 1 mAh cm^{-2}.

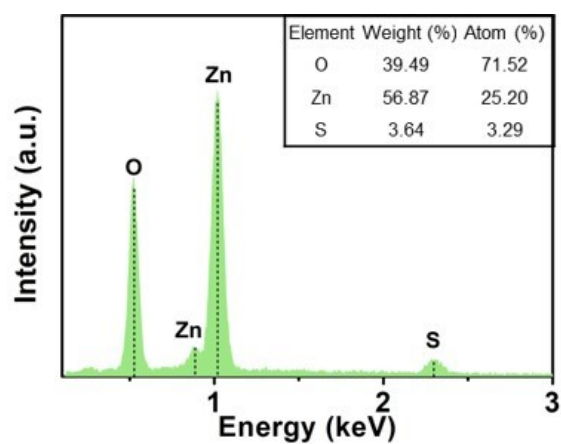| Element	Weight (%)	Atom (%)
O	39.49	71.52
Zn	56.87	25.20
S	3.64	3.29

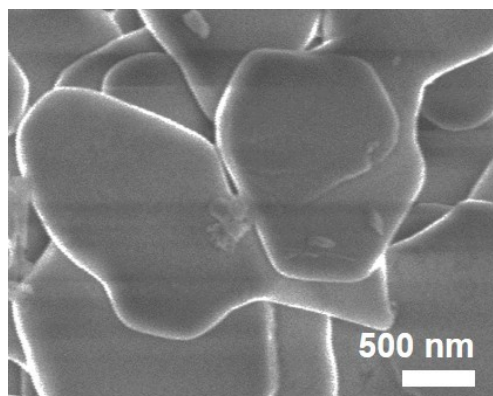**Fig. S5** EDS spectrum of the fragile lamella on the surface of bare Zn.

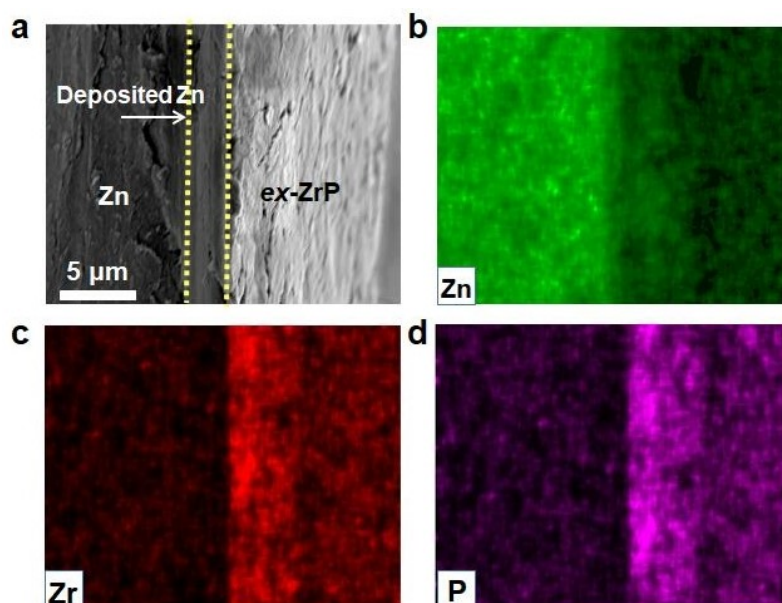**Fig. S6** High-magnification SEM image of Zn/*ex*-ZrP.

Fig. S7 (a) SEM image and (b-d) element maps of Zn/*ex*-ZrP after a Zn-plating of 5 mAh cm^{-2}.

In order to prove the deposition of Zn underneath the artificial layer, Zn plating was conducted on Zn/*ex*-ZrP for 5 mAh cm^{-2}. Then, the electrode was cut into half for cross-section SEM images. As shown in Fig. S7, it can be easily concluded that *ex*-ZrP still locates on the top and the deposited Zn stays below *ex*-ZrP, based on their morphology and element maps. This result is consistent with the poor electron conductivities of *ex*-ZrP and PVdF.

Fig. S8 Contact angle measurements of water on *α*-ZrP, *ex*-ZrP and PVdF.
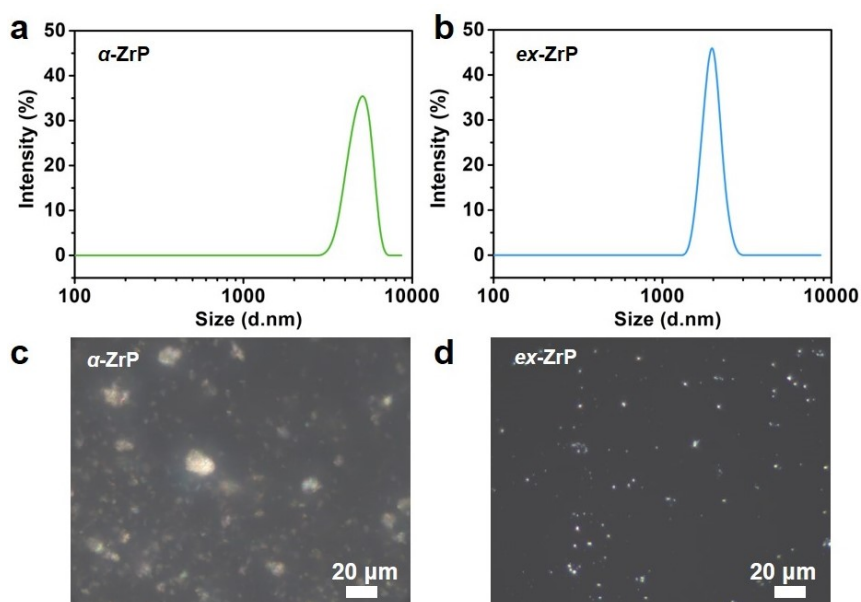

Fig. S9 (a,b) dynamic size analysis and (c,d) optical microscope images of *α*-ZrP and *ex*-ZrP powders dispersed in NMP containing 2 wt% of PVdF.

The help of this intercalation on the dispersion of *ex*-ZrP in PVdF is supported by dynamic size analysis, optical images and SEM images. Compared to that of *α*-ZrP, the smaller dynamic size of *ex*-ZrP in NMP indicates the less aggregation (Fig. S9a, S9b), benefiting the formation of a uniform mixture with PVdF. This conclusion is directly validated by optical images (Fig. S9c, S9d). After the evaporation of NMP, *ex*-ZrP and PVdF leads to a dense and compact layer on Zn foils (Fig. 3i), while *α*-ZrP and PVdF results in a porous layer (Fig. 3e).
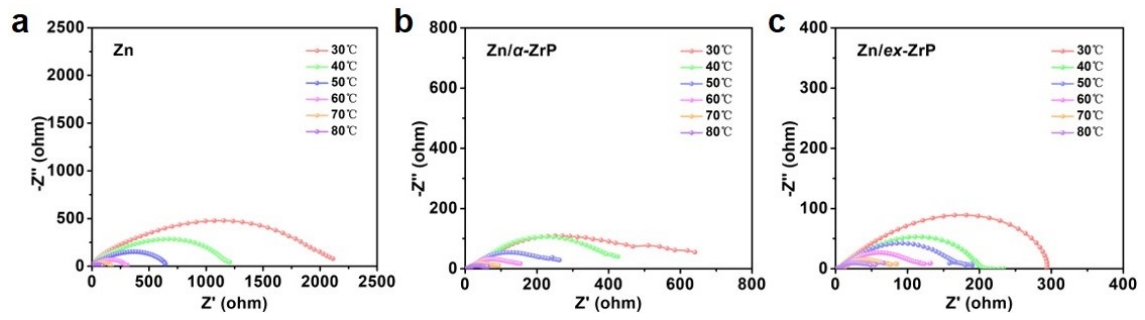
Fig. S10 EIS spectra of bare Zn, Zn/α-ZrP and Zn/*ex*-ZrP at different temperatures.
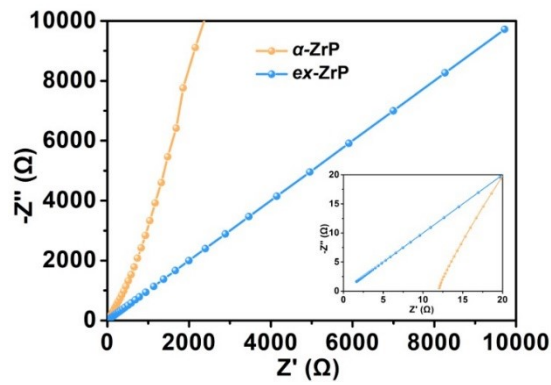

Fig. S11 Nyquist plots of α-ZrP and *ex*-ZrP interface (inset: enlarged area from 0 to 20 ohm).

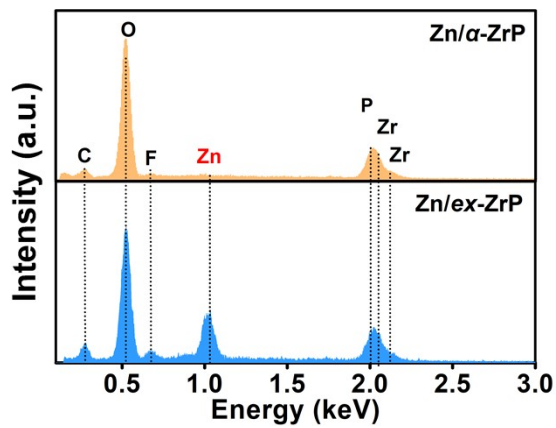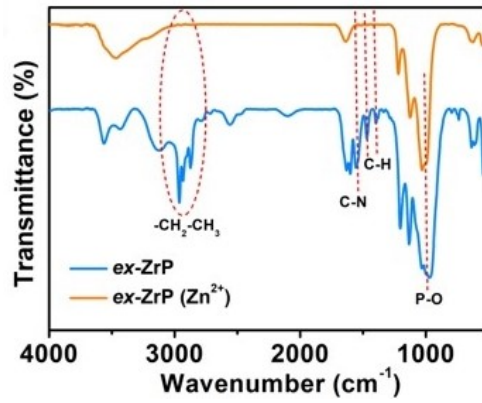**Fig. S12** EDS spectra of Zn/α-ZrP and Zn/*ex*-ZrP after soaking in the electrolyte.

Fig. S13 FT-IR spectra of *ex*-ZrP after soaking in the electrolyte. (Before testing, samples were dried in vacuum at 60 °C for 12 h.）
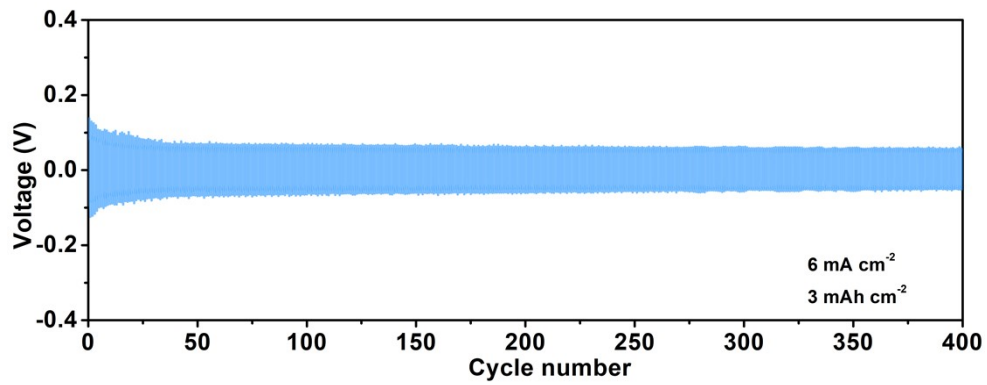
Fig. S14 Cycling performance of Zn/*ex*-ZrP after *n*-butylamine was replaced by Zn^{2+} in symmetric cells.
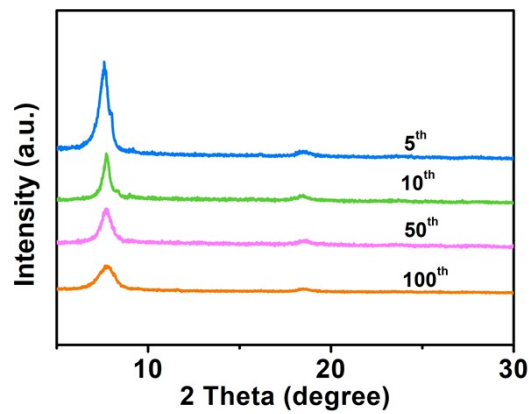
Fig. S15 XRD patterns of Zn/*ex*-ZrP after different cycles.

Fig. S16 HRTEM images of *ex*-ZrP (a) before and (b) after 10 cycles.

Fig. S17 Linear polarization curves and the impedance spectra before and after the measurement. (a) Bare Zn, (b) Zn/α-ZrP, (c) Zn/*ex*-ZrP.

Fig. S18 (a) Initial Zn/*ex*-ZrP foil, (b) rolled Zn/*ex*-ZrP foil, (c) Zn/*ex*-ZrP foil after rolling, (d) folded Zn/*ex*-ZrP foil, and (e) Zn/*ex*-ZrP foil after folding.

Fig. S19 (a) Zn/*ex*-ZrP foil before tape sticking, (b) tape-adhered Zn/*ex*-ZrP foil, (c) Zn/*ex*-ZrP foil after the peeling off tape.
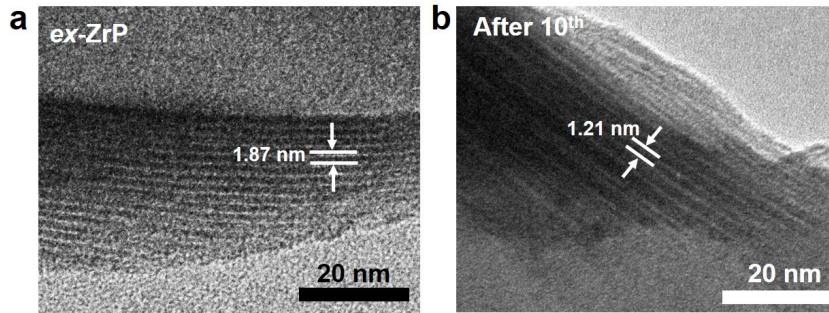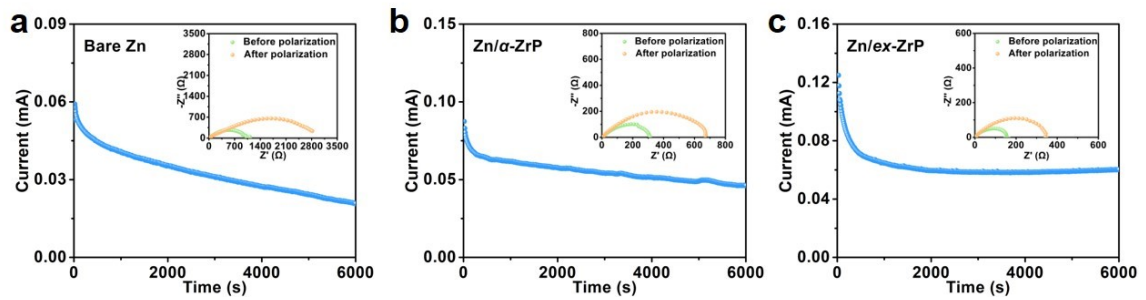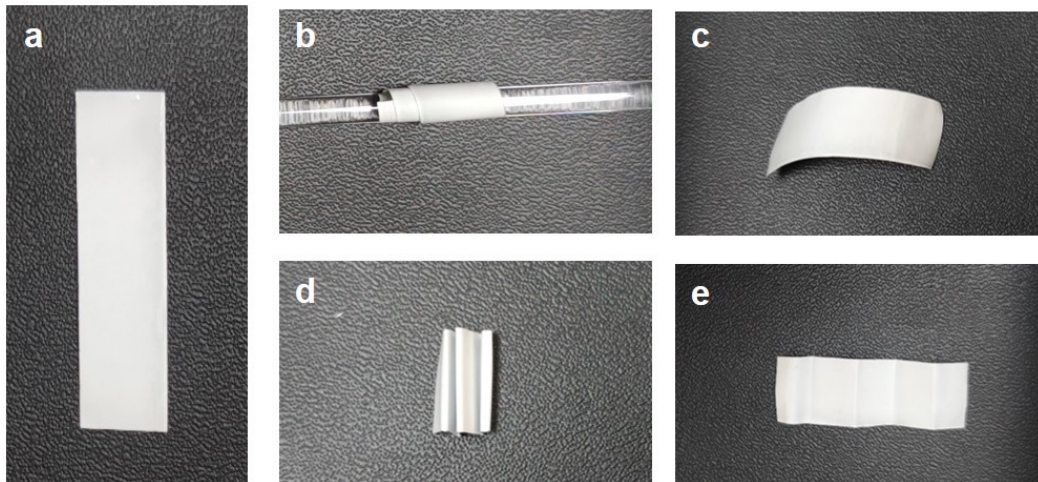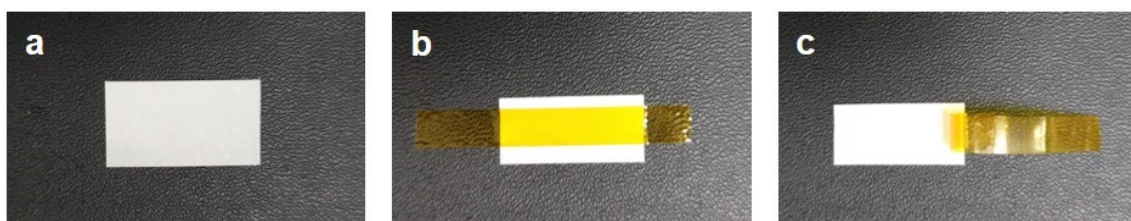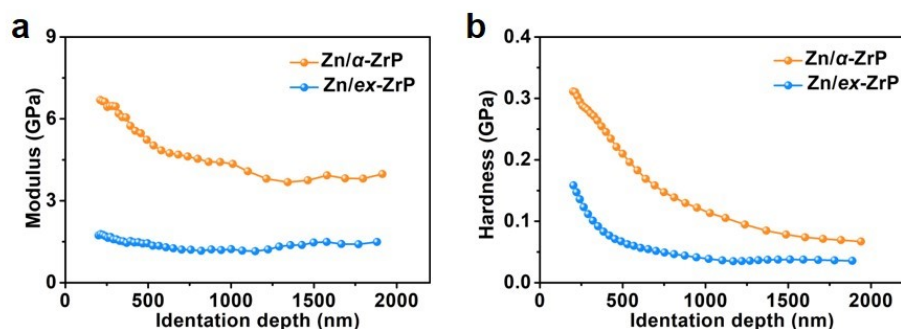

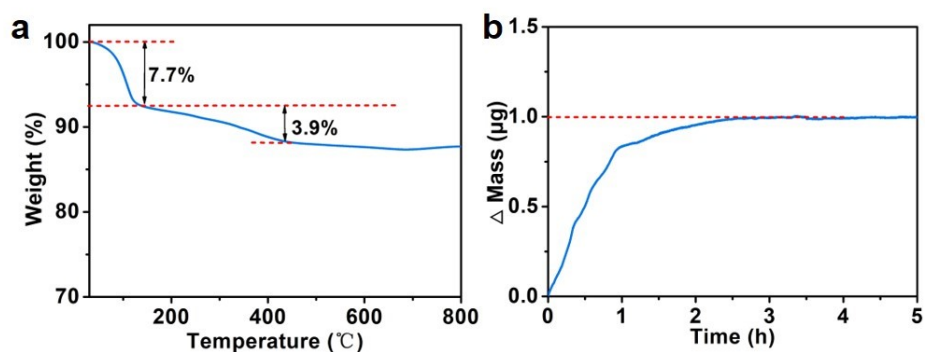**Fig. S20** (a) Elastic modulus and (b) hardness of Zn/*α*-ZrP and Zn/*ex*-ZrP.

Fig. S21 (a) TGA curve of *ex*-ZrP after soaking in the electrolyte, (b) *in-situ* mass change during the soaking of *ex*-ZrP in the electrolyte.

To gain insights about the content of water molecules in the channels of *ex*-ZrP, TGA analysis were measured for *ex*-ZrP powders. *ex*-ZrP was immersed in the electrolyte overnight, and then the remnant electrolyte on the surface was removed by tissue paper carefully. Finally, the electrode was dried at room temperature for hours. As displayed in Fig. S21a, the weight loss in the range of 60-120 °C (7.7 wt%) is likely caused by water molecules adsorbed on the surface.[1] In view of the nanoscale size of *ex*-ZrP and the simple drying at room temperature, such an amount of water adsorption is reasonable. The weight loss around 400 °C (3.9 wt%) is due to escape of water molecules in hydrated zinc ions encapsulated in *ex*-ZrP.[2] Based on this data, the molar ratio of water to Zn^{2+} in hydrated zinc ions can be estimated as 0.59. Therefore, it can be concluded that the majority of water molecules in hydrated zinc ions ($[Zn(H_2O)_6]^{2+}$) are excluded from *ex*-ZrP during the ion-exchange process, but there are still a few of water molecules around Zn^{2+}. This result is also confirmed by *in-situ* quartz crystal microbalance (QCM). QCM can precisely monitor the tiny mass change during the ion-exchange process and clarify the species intercalated into ZrP. As presented in Fig. S21b, the mass gradually increases in the first hour, where n-butylamine diffuse out and partially hydrated zinc ions get in. After that, the mass change levels off, suggesting the completion of this ion-exchange process. Using the mass change, the molar ratio of water to Zn^{2+} in partially hydrated zinc ions is 0.36, comparable to that obtained from TG analysis.
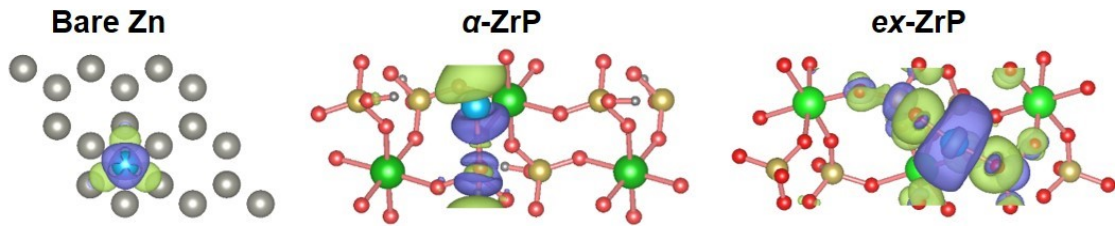
Fig. S22 Charge density differences of Zn atoms adsorbed on different layer, where light green and purple areas represent positive and negative charge differences.
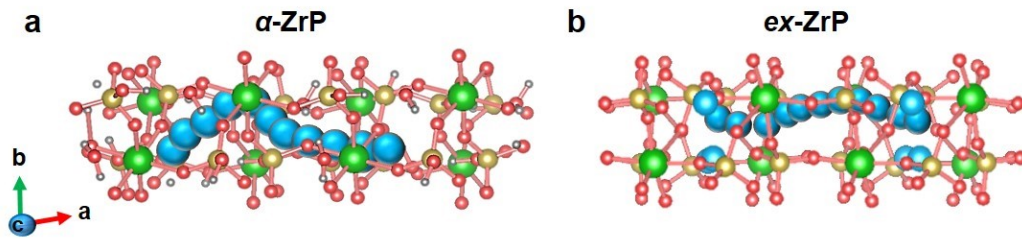

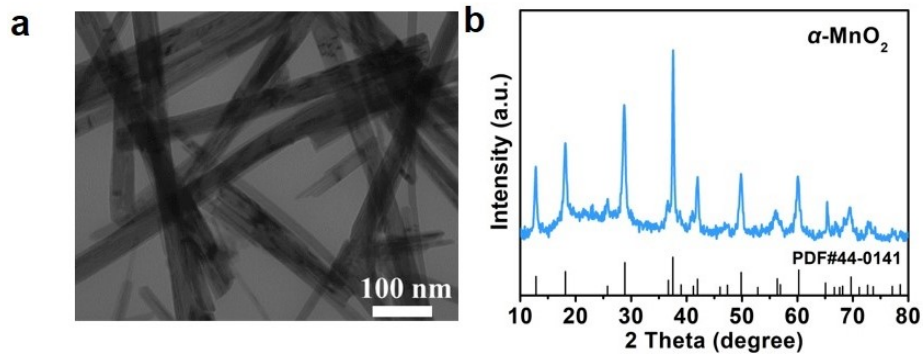**Fig. S23** Top view of Zn diffusion paths in α-ZrP and ex-ZrP.
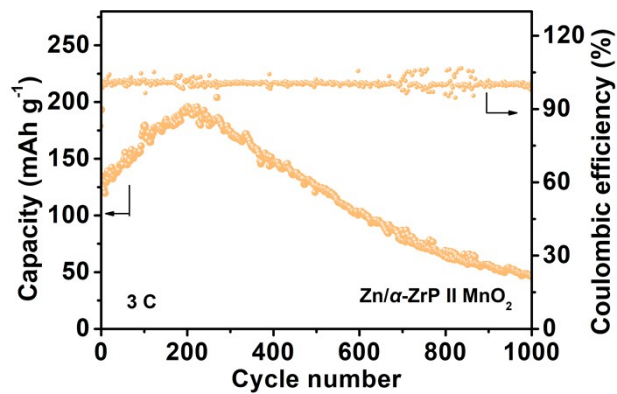

Fig. S24 (a) TEM image and (b) XRD pattern of α-MnO$_2$.

Fig. S25 Cycling performances of Zn/α-ZrP||α-MnO$_2$.
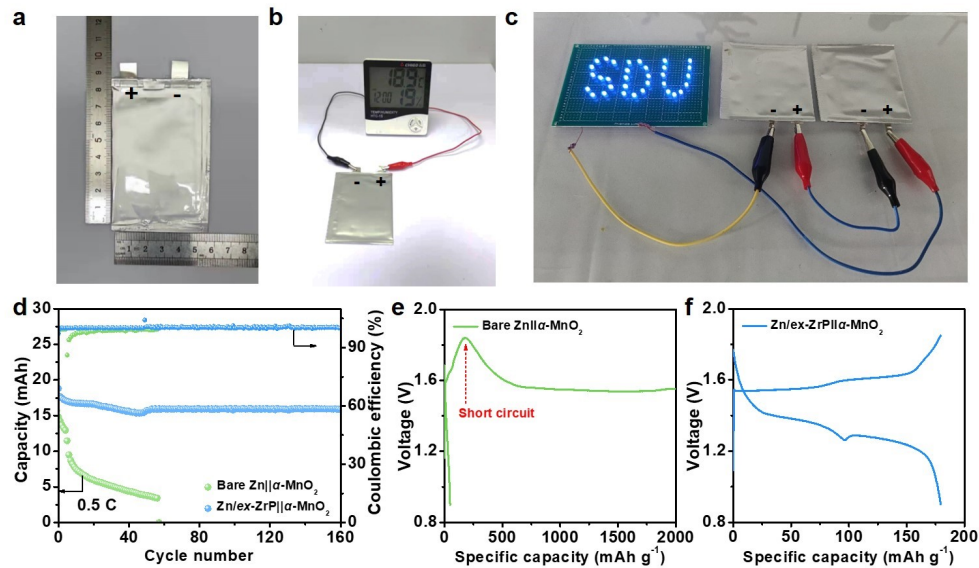
Fig. S26 (a) Optical photos of Zn/ex-ZrP||α-MnO$_2$ pouch cell. (b, c) Photograph of a pouch cell powering a liquid-crystal display and LED light. (d) Long-term cycling performances of large-capacity bare Zn||MnO$_2$ and Zn/ex-ZrP||MnO$_2$ full cells. (e, f) Galvanostatic discharge/charge profiles of bare Zn||α-MnO$_2$ and Zn/ex-ZrP||α-MnO$_2$.

Fig S26d shows that the pouch cell of bare Zn||α-MnO$_2$ rapid fades in capacity than Zn/ex-ZrP||α-MnO$_2$. The capacity decay is more severe than that in coin cells, which could be correlated to the structure difference between pouch cells and coin cells. In pouch cells, the current spreads out along the electrode through "tabs", which results in the in-plane resistance for electron transport and considerable ohmic loss[3]. This ohmic loss increases with the size of pouch cells and results in a significant voltage gradient on current collectors. Therefore, the uneven distribution of voltage and current in large-sized pouch cells promotes the formation of Zn dendrites, eventually leading to inferior electrochemical performances. This result is also supported by the voltage profiles, as shown in Fig. S26e. The short circuit induced by Zn dendrites is clearly observed for bare Zn||α-MnO$_2$. As for Zn/ex-ZrP||α-MnO$_2$, the voltage profiles are kept almost the same as before (Fig. S26f).

Fig. S27 The formation of ex-V$_2$O$_5$ obtained by treating V$_2$O$_5$ with polyaniline (PANI).

Fig. S28 (a) XRD patterns and (c) FTIR spectra of V_2O_5 and *ex*-V_2O_5.
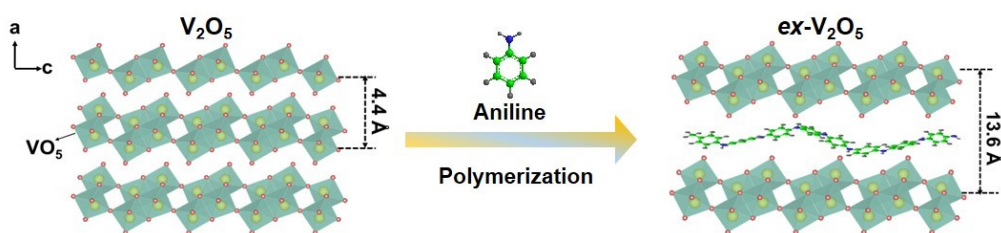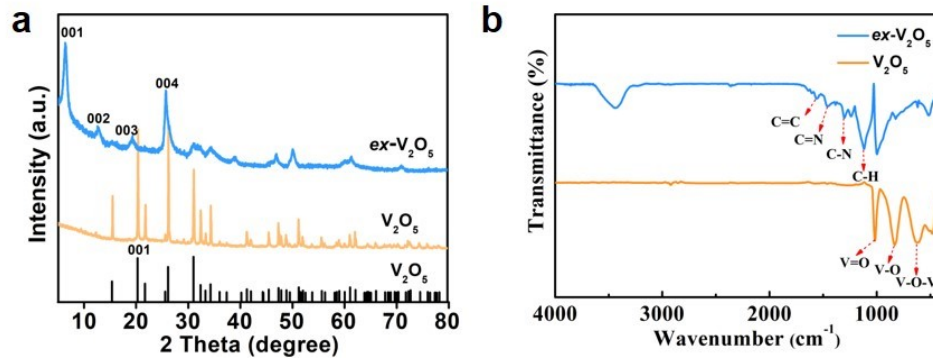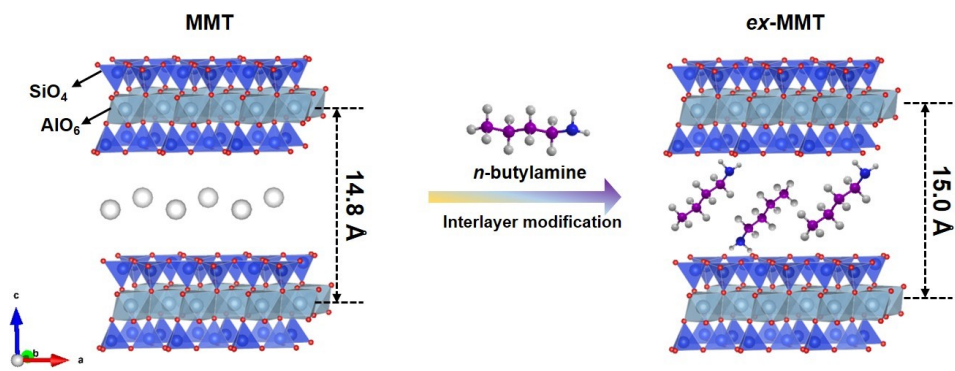

Fig. S29 The formation of *ex*-MMT obtained by treating MMT with *n*-butylamine.
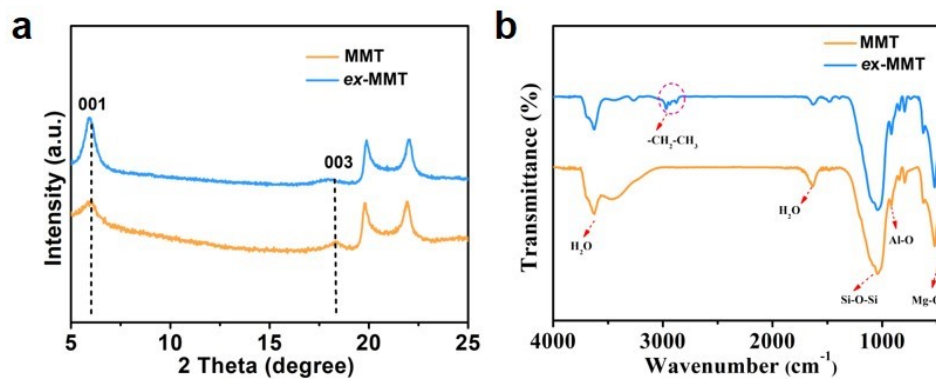
Fig. S30 (a) XRD patterns and (c) FTIR spectra of MMT and *ex*-MMT.

Table S1 EDS results of Zn/α-ZrP and Zn/ex-ZrP after soaking in electrolytes.

Element	Zn/α-ZrP (wt%)	Zn/ex-ZrP (wt%)
C	9.78	8.99
F	3.02	2.91
O	36.04	33.18
P	19.54	13.07
Zr	29.7	20.78
Zn	1.91	21.06

Table S2 Cycling performances of the symmetrical cells using different artificial layers on Zn.

Coating materials	Current density (mA cm^{-2})	Capacity (mA h cm^{-2})	Cycle number	References
MXene	0.2	0.2	400	4
CaCO$_3$	0.25	0.05	2000	5
MOF	0.5	0.5	1500	6
Poly (vinyl butyral)	0.5	0.5	1100	7
TiO$_2$	0.885	0.885	1000	8
MOF-PVdF	1	0.5	500	9
Al$_2$O$_3$	1	1	250	10
Indium (In)	1	1	250	11
NaTi$_2$(PO$_4$)$_3$	1	1	120	12
ZnS	2	2	500	13
Sc$_2$O$_3$	2	2	120	14
Carbon	2.5	1	300	15
Kaolin	4.4	1.1	1600	16
3D nanoporous ZnO	5	1.25	1000	17
MMT	1	0.25	1000	18
Mont	2	1	700	19
ex-ZrP	6	1	3000	This work
ex-ZrP	6	3	450	This work
ex-MMT	6	3	900	This work

Table S3 Cycling performances of the full cells using different artificial layers on Zn anodes.

Cathode	Anode	Current density (mA g^{-1})	Capacity (mA h g^{-1})	Capacity retention (%)	References
MnO$_2$	MOF-PVdF@Zn	30.8	200	100% after 50 cycles	9
MnO$_2$	KL-Zn	500	210	90.4% after 600 cycles	16
MnO$_2$	PA@Zn	600	176.1	88% after 1000 cycles	20
MnO$_2$	AEC-Zn	616	256	91.4% after 300 cycles	8
MMT-MnO$_2$	MMT-Zn	616	210	90% after 1000 cycles	18
MnO$_2$	MOF@Zn	700	180.3	88.9% after 600 cycles	6
MnO$_2$	Zn/C$_3$N$_4$	1000	130	94.4% after 500 cycles	21
MnO$_2$	F-TiO$_2$@Zn	1000	100	84.1% after 300 cycles	22
MnO$_2$	CaCO$_3$@Zn	1000	206	86% after 1000 cycles	5
MnO$_2$	BTO@Zn	650	151	72.6% after 1000 cycles	23
MnO$_2$	Zn/*ex*-ZrP	924	180	95% after 1500 cycles	This work

References

1. W. Mu, Q. Yu, J. Gu, X. Li, Y. Yang, H. Wei, S. Peng, *Sep. Purif. Technol.,* 2020, **240**, 116658.

2. H. Xiao, W. Dai, Y. Kan, A. Clearfield, H. Liang, *Appl. Surf. Sci.,* 2015, **329**, 384-389.

3. S. H. Park, S. Y. Byeon, J. H. Park, C. Kim, *ACS Energy Lett.,* 2021, **6**, 3078-3085.

4. N. Zhang, S. Huang, Z. Yuan, J. Zhu, Z. Zhao, Z. Niu, *Angew. Chem. Int. Ed.,* 2021, **60**, 2861-2865.

5. L. Kang, M. Cui, F. Jiang, Y. Gao, H. Luo, J. Liu, W. Liang and C. Zhi, *Adv. Energy Mater.*, 2018, **8**, 1801090.

6. H. Yang, Z. Chang, Y. Qiao, H. Deng, X. Mu, P. He and H. Zhou, *Angew. Chem. Int. Ed.*, 2020, **59**, 9377-9381.

7. J. N. Hao, X. L. Li, S. L. Zhang, F. H. Yang, X. H. Zeng, S. Zhang, G. Y. Bo, C. S. Wang and Z. P. Guo, *Adv. Funct. Mater.*, 2020, **30**, 2001263.

8. R. Zhao, Y. Yang, G. Liu, R. Zhu, J. Huang, Z. Chen, Z. Gao, X. Chen and L. Qie, *Adv. Funct. Mater.*, 2020, **31**, 2001867.

9. M. Liu, L. Yang, H. Liu, A. Amine, Q. Zhao, Y. Song, J. Yang, K. Wang and F. Pan, *ACS Appl. Mater. Interfaces*, 2019, **11**, 32046-32051.

10. H. He, H. Tong, X. Song, X. Song and J. Liu, *J. Mater. Chem. A*, 2020, **8**, 7836-7846.

11. D. Han, S. Wu, S. Zhang, Y. Deng, C. Cui, L. Zhang, Y. Long, H. Li, Y. Tao, Z. Weng, Q. H. Yang and F. Kang, *Small*, 2020, **16**, 2001736.

12. M. Liu, J. Cai, H. Ao, Z. Hou, Y. Zhu and Y. Qian, *Adv. Funct. Mater.*, 2020, **30**, 2004885.

13. J. Hao, B. Li, X. Li, X. Zeng, S. Zhang, F. Yang, S. Liu, D. Li, C. Wu and Z. Guo, *Adv. Mater.*, 2020, **32**, 2003021.

14. M. Zhou, S. Guo, G. Fang, H. Sun, X. Cao, J. Zhou, A. Pan and S. Liang, *J. Energy Chem.*, 2021, **55**, 549-556.

15. W. Li, K. Wang, M. Zhou, H. Zhan, S. Cheng and K. Jiang, *ACS Appl. Mater. Interfaces*, 2018, **10**, 22059-22066.

16. C. B. Deng, X. S. Xie, J. W. Han, Y. Tang, J. W. Gao, C. X. Liu, X. D. Shi, J. Zhou and S. Q. Liang, *Adv. Funct. Mater.*, 2020, **30**, 2000599.

17. X. Xie, S. Liang, J. Gao, S. Guo, J. Guo, C. Wang, G. Xu, X. Wu, G. Chen and J. Zhou, *Energy Environ. Sci.*, 2020, **13**, 503-510.

18. H. B. Yan, S. M. Li, Y. Nan, S. B. Yang and B. Li, *Adv. Energy Mater.*, 2021, **11**, 2100186.

19. L. Hong, X. M. Wu, C. Ma, W. Huang, Y. F. Zhou, K. X. Wang and J. S. Chen, *J. Mater. Chem. A*, 2021, **9**, 16814-16823.

20. Z. Zhao, J. Zhao, Z. Hu, J. Li, J. Li, Y. Zhang, C. Wang and G. Cui, *Energy Environ. Sci.*, 2019, **12**, 1938-1949.

21. P. Liu, Z. Zhang, R. Hao, Y. Huang, W. Liu, Y. Tan, P. Li, J. Yan and K. Liu, *Chem. Eng. J.*, 2021, **403**, 126425.

22. Q. Zhang, J. Luan, X. Huang, Q. Wang, D. Sun, Y. Tang, X. Ji and H. Wang, *Nat. Commun.*, 2020, **11**, 3961.

23. P. Zou, R. Zhang, L. Yao, J. Qin, K. Kisslinger, H. Zhuang, H. L. Xin, *Adv. Energy Mater.* 2021, *11*, 2100982.